Multiharmonic Frequency-Chirped Transducers for Surface-Acoustic-Wave Optomechanics

Matthias Weiß,[1,2] Andreas L. Hörner,[1] Eugenio Zallo,[3,†] Paola Atkinson,[3,4] Armando Rastelli,[5,3] Oliver G. Schmidt,[3] Achim Wixforth,[1,2,6] and Hubert J. Krenner[1,2,6,*]

[1]*Lehrstuhl für Experimentalphysik 1 and Augsburg Centre for Innovative Technologies (ACIT), Universität Augsburg, Universitätsstraße 1, 86159 Augsburg, Germany*
[2]*Nanosystems Initiative Munich (NIM), Schellingstraße 4, 80339 München, Germany*
[3]*Institute for Integrative Nanosciences, Leibniz IFW Dresden, Helmholtzstraße 20, 01069 Dresden, Germany*
[4]*Institut des NanoSciences de Paris, Sorbonne Universités, UPMC Université Paris 06, CNRS UMR7588, 4 Place Jussieu, F-75005 Paris, France*
[5]*Institute of Semiconductor and Solid State Physics, Johannes Kepler Universität Linz, Altenbergerstraße 69, 4040 Linz, Austria*
[6]*Center for Nanoscience (CeNS), Ludwig-Maximilians-Universität München, Geschwister-Scholl-Platz 1, 80539 München, Germany*

(Received 1 August 2017; revised manuscript received 29 October 2017; published 8 January 2018)

Wide-passband interdigital transducers are employed to establish a stable phase lock between a train of laser pulses emitted by a mode-locked laser and a surface acoustic wave generated electrically by the transducer. The transducer design is based on a multiharmonic split-finger architecture for the excitation of a fundamental surface acoustic wave and a discrete number of its overtones. Simply by introducing a variation of the transducer's periodicity p, a frequency chirp is added. This combination results in wide frequency bands for each harmonic. The transducer's conversion efficiency from the electrical to the acoustic domain is characterized optomechanically using single quantum dots acting as nanoscale pressure sensors. The ability to generate surface acoustic waves over a wide band of frequencies enables advanced acousto-optic spectroscopy using mode-locked lasers with fixed repetition rate. Stable phase locking between the electrically generated acoustic wave and the train of laser pulses is confirmed by performing stroboscopic spectroscopy on a single quantum dot at a frequency of 320 MHz. Finally, the dynamic spectral modulation of the quantum dot is directly monitored in the time domain combining stable phase-locked optical excitation and time-correlated single-photon counting. The demonstrated scheme will be particularly useful for the experimental implementation of surface-acoustic-wave-driven quantum gates of optically addressable qubits or collective quantum states or for multicomponent Fourier synthesis of tailored nanomechanical waveforms.

DOI: 10.1103/PhysRevApplied.9.014004

I. INTRODUCTION

The realization of hybrid quantum systems [1,2] is guided by the vision to exploit the strengths of individual constituents, while at the same time bypassing their detrimental shortcomings. In this quest at the forefront of contemporary fundamental and applied research, mechanical systems stand out: vibrational excitations and phonons couple to virtually any type of quantum system. In condensed matter, a wide range of qubit systems has been successfully interfaced with localized and narrow-band vibrational modes [3–7]. For a full-fledged quantum circuitry in which qubits are interconnected via mechanical links, surface acoustic waves (SAWs) are of paramount importance. SAWs can be elegantly excited directly on piezoelectric materials using so-called interdigital transducers (IDTs) [8] and are weakly susceptible only to dissipation. The periodicity p of such interdigitating combs of electrodes determines the frequency of the excited SAW $f_{\mathrm{SAW}} = c_{\mathrm{SAW}}/2p$, with c_{SAW} being the SAW phase velocity in the material along the SAW propagation direction. Key wave phenomena can be directly employed using these surface-confined mechanical waves. For instance, the generation of arbitrary dynamic nanomechanical waveforms has been realized very recently by additive Fourier

*hubert.krenner@physik.uni-augsburg.de
†Present address: Paul-Drude-Institut für Festkörperelektronik, Hausvogteiplatz 5-7, 10117 Berlin, Germany.

synthesis [9]. Similarly, acoustic Bragg resonators have been realized. Because of the SAW's low phase velocity, typically ranging $c_{\mathrm{SAW}} \approx 3000 - 7000$ m/s, high-quality SAW resonators are widely used as small and compact radio-frequency filters [10,11], which are indispensable in modern wireless communication networks. This application makes SAWs a *phononic* technology of highest industrial relevance.

For more than the past 30 years, SAWs also have been advanced towards a versatile probe and manipulation tool in fundamental research. Examples include the investigation of collective quantum effects such as the quantum Hall effects [12–14] and acoustic transport of charges [15–20] and spins [21,22] in low-dimensional semiconductor nanosystems. Recently, SAWs have been successfully interfaced with single quantum systems, individual charges [23–25] and spins [26], or superconducting quantum bits [27]. In addition to these electrically addressable quantum systems, optically active systems are of paramount importance, as these allow us to transduce excitations from the acoustic domain at hypersonic frequencies in the 100-MHz to the low-gigahertz range to the optical domains at frequencies of hundreds of terahertz. In this area, single optically active quantum dots (QDs) and defect centers [28] and photonic [29–32] and optomechanical cavities [33–36] have been in focus. On the one hand, acoustically regulated carrier injection may be used to deliver a precisely triggered train of single photons [37–39] from discrete states in a QD programmed by the SAW [40–44]. On the other hand, the dynamic mechanical displacement and its resulting strain lead to a spectral modulation of the emitter due to deformation potential coupling [45], even in the resolved sideband regime [46,47]. These recent breakthroughs in the deliberate coupling of single quantum systems to propagating SAWs were put on a solid theoretical foundation of SAW-based quantum acoustics [48] in which SAW phonons take the role of microwave photons. Albeit such quantum acoustics can be readily implemented with superconducting qubits or single electron spins, which exhibit resonances precisely in this frequency range, transduction to optical frequencies requires novel strategies and methodologies. As one key requirement to implement SAW-driven quantum gates with optically active nanosystems, e.g., based on Landau-Zener transitions in a coupled-quantum-dot nanocavity system [49,50], the SAW has to be phase locked to a train of laser pulses. Such quantum gates typically require resonant excitation with highly coherent pulses emitted by a mode-locked-laser system, whose pulse repetition rate is fixed. Thus, stable phase locking between the SAW, whose frequency is set by the IDT's periodicity, and these laser pulses is a challenging task.

Here we report on the application of a wide-passband IDT architecture to establish a stable phase lock between a SAW and a train of laser pulses for advanced acousto-optic spectroscopy of single QDs. Our IDT design is based on a multiharmonic split-finger architecture [9] for the excitation of a fundamental SAW and a well-defined number of overtones. It is combined with a frequency chirp [51] by introducing a variation of the IDT's periodicity p. This combination results in wide frequency bands for each harmonic, which we characterize optomechanically using single-sensor QDs. Most important, we show that SAWs can be generated by the frequency-filtered electrical monitor signal of a free-running mode-locked laser, giving rise to natively stable phase locking between the train of laser pulses and the generated SAW. We introduce both electrical and optical delays and tune the relative phase for stroboscopy. Finally, we realize full-fledged SAW spectroscopy of a single QD. In this scheme, we combine phase-locked excitation with high spectral and high temporal resolution and monitor the dynamic spectral modulation of the QD emission line on subnanosecond time scales.

II. EXPERIMENTAL IMPLEMENTATION

A schematic of our device is depicted in Fig. 1(a). It is comprised of IDTs patterned directly on an (Al,Ga)As heterostructure containing a single layer of strain-free

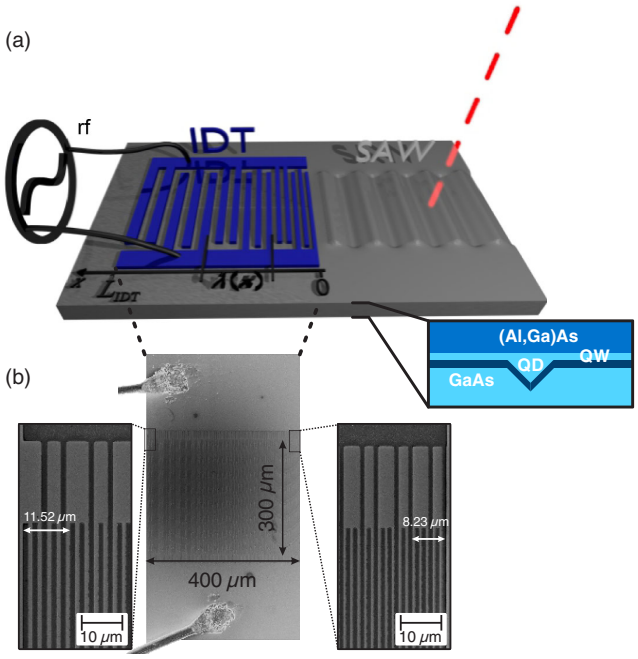

FIG. 1. Device layout and optomechanical sensing using a sensor QD. (a) Left: Device layout consisting of a metal IDT patterned onto an (Al,Ga)As-based heterostructure. The IDT design combines a split-52 electrode configuration for multiharmonics generation and a variation of the periodicity p of the fingers of the IDT. This geometric change gives rise to a variation of the wavelength of the generated SAW along the axis x of the IDT $[2p = \lambda(x)]$. The x direction corresponds to the [110] crystal direction of the (Al,Ga)As heterostructure. (Right) The heterostructure contains a single layer of sensor QDs. These are interrogated optically and detect optomechanically the local pressure induced by a propagating SAW. (b) SEM image of the full IDT (center) and enlargements of the regions at which the long-wavelength (left) and short-wavelength SAWs (right) are generated.

TABLE I. IDT design parameters.

	$f_{\mathrm{SAW},1}$	$\Delta f_{\mathrm{SAW},1}$	λ_0	α	L_{IDT}	A_{IDT}
IDT1	250 MHz	50 MHz	9.6 μm	4.8×10^{-3}	400 μm	300 μm
IDT2	250 MHz	100 MHz	8.23 μm	8.225×10^{-3}	400 μm	300 μm

GaAs/(Al, Ga)As QDs [52]. Details on the heterostructure can be found in Appendix A. The design of the IDTs is based on a split-52 configuration, which allows for the excitation of a fundamental SAW and three overtones harmonics $f_{\mathrm{SAW},n} = nf_{\mathrm{SAW},1}$, with $f_{\mathrm{SAW},1} = 250$ MHz and $n = 1, 2, 3, 4$ [9]. We combine this design with a frequency chirp [53] by introducing a linear variation of the fundamental periodicity

$$2p(x) = \lambda_1(x) = \lambda_0 + \alpha x \tag{1}$$

along the IDT axis. In this equation, α is the dimensionless chirp parameter and $0 \le x \le L_{\mathrm{IDT}}$, with L_{IDT} being the length of the IDT structure. Thus, in the frequency domain, the IDT's fundamental resonance and higher harmonics become

$$f_{\mathrm{SAW},n}(x) = \frac{nc_{\mathrm{SAW}}}{\lambda_1(x)} = \frac{nc_{\mathrm{SAW}}}{(\lambda_0 + \alpha x)}. \tag{2}$$

$c_{\mathrm{SAW}} \approx 2920$ m/s is the phase velocity of the SAW along the [110] direction of the GaAs (001) surface. Moreover, the introduction of a chirp broadens the range of frequencies over which the IDT transduces power between the electrical and acoustic domains to $\Delta f_{\mathrm{SAW},n} = \{[(c_{\mathrm{SAW}})/\lambda_0] - [(c_{\mathrm{SAW}})/\lambda_0 + \alpha L_{\mathrm{IDT}}]\}$. For our experiments, we use two different IDTs: IDT1 and IDT2 with $\Delta f_{\mathrm{SAW},1} = 50$ MHz and $\Delta f_{\mathrm{SAW},1} = 100$ MHz, respectively. The aperture of both IDTs, i.e., the length of the overlapping IDT fingers, is $A_{\mathrm{IDT}} = 300$ μm; see Fig. 1(b). The full sets of design parameters for both IDTs are summarized in Table I. The variation of the IDT period can be nicely seen from the scanning electron micrograph recorded at both ends of IDT2, which are presented in Fig. 1(b).

The embedded QDs act as nanoscale pressure sensors and detect the local hydrostatic pressure of a SAW via the deformation potential coupling [45]. These QDs are dynamically strained by the SAW, which gives rise to a spectral broadening of the emission line. The employed (Al, Ga)As/GaAs QDs are particularly suited for pressure sensing because emission lines can be observed over the full acoustic cycle [9]. This is in stark contrast to the more established self-assembled (In,Ga)As QDs nucleating on a wetting layer, which forms a two-dimensional transport channel [42,54]. The QDs studied here are almost perfectly decoupled from a continuum of states, in which spatio-temporal carrier dynamics can be induced by the SAW. Thus, carriers are expected to be captured on a tens of picoseconds time scale after photoexcitation [55,56], and reprogramming of the QD's charge state by the SAW is inhibited.

Figure 2(a) illustrates the underlying physics: the Lorentzian emission line (gray) of the QD is spectrally tuned by the SAW's strain field as time evolves over on the SAW cycle. By averaging the full acoustic cycle, this dynamic sinusoidal spectral modulation gives rise to a broadening of the emission line. In a time-integrated experiment averaging over $T_{\mathrm{SAW}} = 1/f_{\mathrm{rf}}$, the broadening is given by

$$I(E) = I_0 + f_{\mathrm{rf}}\frac{2A}{\pi}\int_0^{1/f_{\mathrm{rf}}} \frac{w}{4\{E - [\Delta E \sin(2\pi f_{\mathrm{rf}} t)]\}^2 + w^2} dt. \tag{3}$$

In this expression, E denotes the energy relative to the center of the unperturbed line E_0, A the integrated intensity in the absence of the SAW, f_{rf} the frequency of the applied electrical voltage signal, and ΔE the spectral broadening induced by the SAW-modulated deformation potential coupling. The resulting broadened emission line is plotted in green in Fig. 2(a). From this analysis, we evaluate the spectral modulation amplitude $\Delta E(f_{\mathrm{rf}})$ and, thus, quantify the local hydrostatic pressure at the position of the QD.

In Fig. 2(b), we demonstrate nanoscale sensing of the SAW's acoustic field. We compare the measured

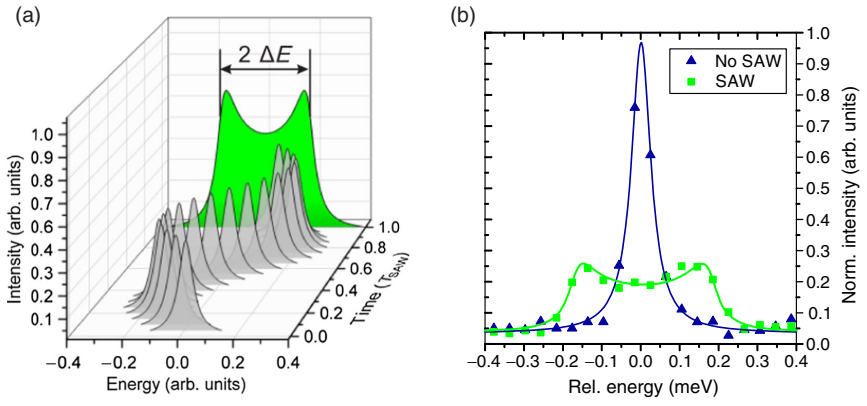

FIG. 2. Nanoscale pressure sensing. (a) Expected dynamic sinusoidal spectral tuning of a Lorentzian emission line (gray) over one acoustic cycle induced by the SAW's strain field. Integration over all times during the full cycle results in the green averaged spectrum. From fitting Eq. (3), the amplitude of the dynamic broadening ΔE can be extracted. (b) Emission of a single QD without a SAW applied (blue symbols) and strained by an 801-MHz SAW (green symbols). Solid lines are best fits of Eq. (3) to the experimental data.

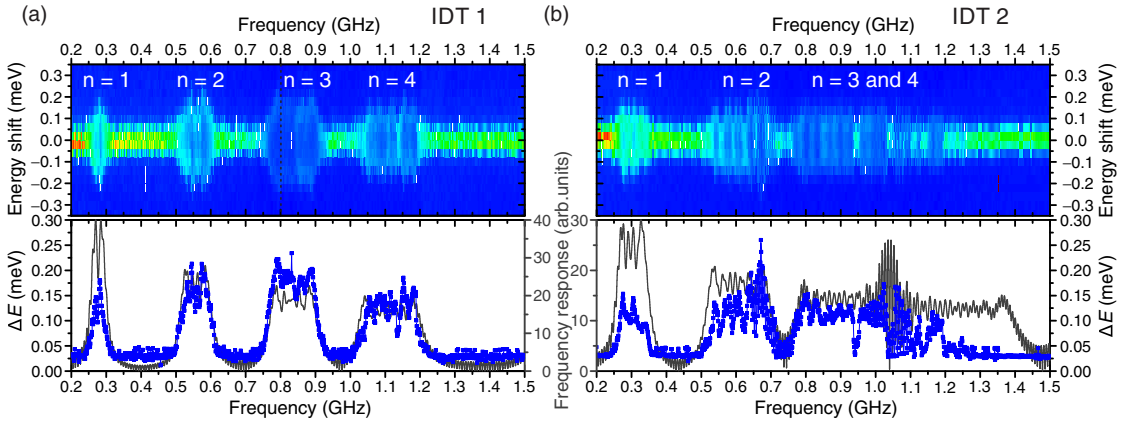

FIG. 3. Optomechanical characterization of IDTs. Upper panels: False-color plot of the normalized emission intensity as a function of f_{rf} and ΔE for IDT1 (a) and IDT2 (b) showing clear spectral broadening of the emission line at the characteristic frequency bands $n = 1$, 2, 3, 4 of each IDT. In (a), the dashed vertical line marks the spectrum of the modulated QD shown in Fig. 1(c). Lower panels: ΔE (blue symbols) derived from the data in the upper panels and calculated frequency response (gray solid line) of IDT1 (a) and IDT2 (b).

time-integrated emission spectra (symbols) of a single QD without (blue) and with (green) a SAW applied. The energy axis is referenced to the center energy of the unperturbed emission line. In the latter case, the QD's Lorentzian emission line is spectrally tuned with frequency $f_{\mathrm{SAW}} = 801$ MHz by the time-modulated deformation potential coupling.

We characterize the SAW generation of both IDTs by measuring the emission spectrum of a single QD as we sweep the radio frequency f_{rf} of the output voltage of a rf signal generator, while keeping the rf power-level constant at $P_{\mathrm{rf}} = +24$ dBm (approximately 250 mW). The upper panels of Figs. 3(a) and 3(b) show the results of such frequency sweeps for IDT1 and IDT2, respectively. The normalized emission intensity is color coded with red (blue) colors corresponding to high (low) intensity and plotted as a function of f_{rf} and photon energy shift relative to the unperturbed QD emission energy E_0. E_0 is corrected for a small shift of the center energy due to a variation of the thermal load as f_{rf} is tuned, which is measured independently at the times the SAWs pass by the QD's position [57]. For both IDTs, we observe a pronounced spectral broadening of the QD emission line over broad ranges of f_{rf} for all harmonics expected for our split-52 configuration. The observed broadening is larger for IDT2 compared to that for IDT1, which directly reflects the larger value of the chirp parameter α (see Table I) and the resulting $\Delta f_{\mathrm{SAW},n}$. Furthermore, the linear dependence $\Delta f_{\mathrm{SAW},n} \propto f_{\mathrm{SAW},n} \propto n$ is nicely resolved for the fundamental SAW and its overtones for each IDT. For IDT2, the $n = 3$ and $n = 4$ frequency bands overlap, giving rise to a quasicontinuous band, over which SAWs can be generated. In such an experiment, we are able to directly assess the frequency-dependent SAW conversion efficiency of an IDT by fitting the experimentally measured line shape using Eq. (3) of Ref. [58]. In the lower panels of Figs. 3(a) and 3(b), we plot the extracted spectral broadening $\Delta E(f_{\mathrm{rf}})$ of the sensor QD emission line (blue symbols) and the calculated frequency response of the two IDTs (black line) as a function of f_{rf}. To model the frequency response of the IDT, we use an impulse model [59,60] detailed in Appendix B. Clearly, the optomechanically measured frequency response nicely agrees with our simulation for IDT1. For IDT2, the isolated frequency bands $n = 1$ and $n = 2$ show good agreement between experiment and simulation. For $n = 3$ and $n = 4$, the experimental data exhibit a complex interference pattern. For $f_{\mathrm{rf}} \gtrsim 920$ MHz, it differs from that expected from our basic impulse IDT model.

In our chirped transducer design, different $f_{\mathrm{SAW},n}(x)$ are generated at well-defined positions x along the IDT axis. This effect is shown schematically in Fig. 4(a). For our design, the corresponding propagation length scales with the SAW frequency as

$$\Delta x = \frac{n c_{\mathrm{SAW}}}{\alpha} \frac{1}{f_{\mathrm{SAW},n}} - \frac{\lambda_0}{\alpha}. \tag{4}$$

Figure 4(b) shows the measured Δx as a function of $f_{\mathrm{SAW},1}$ of the fundamental resonance band of IDT1. The measured data (symbols) confirm the expected dependence for our design. The red curve is a best fit of Eq. (4) to the data. From this fit, we derive $\alpha = (4.9 \pm 0.6) \times 10^{-3}$. This value agrees well within the experimental error with the nominal design value of 4.8×10^{-3} (cf. Table I).

III. STROBOSCOPIC SPECTROSCOPY WITH TIME-INTEGRATED DETECTION

We employ the demonstrated *broadband* excitation of SAWs to establish a stable and programmable phase relation between the sound wave and the train of pulses of a mode-locked laser. To ensure a stable phase lock, the

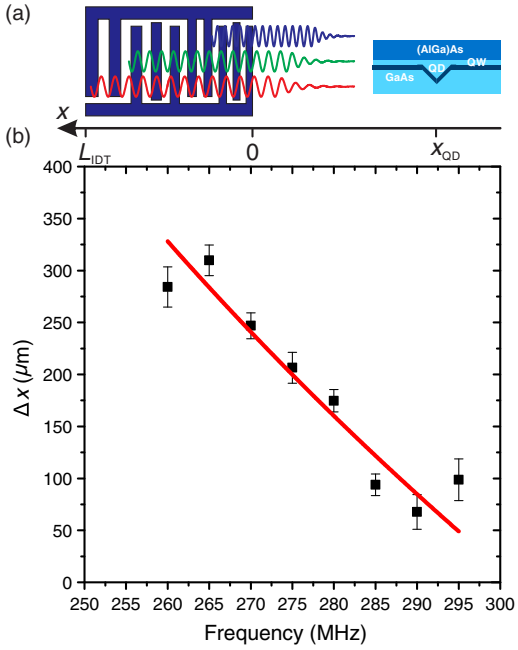

FIG. 4 Local SAW generation in a chirped transducer. (a) Illustration of the frequency-dependent variation of the SAW's propagation length Δx from the point of excitation along the axis of the IDT (left) to the fixed position of the sensor QD. (b) Measured Δx as a function of frequency across the $f_{\mathrm{SAW},1}$ band of IDT1 (symbols) and best fit of Eq. (4) to the data.

laser repetition rate f_{laser} and f_{SAW} have to be harmonics, $f_{\mathrm{SAW}} = m f_{\mathrm{laser}}$, m an integer. To meet this strict criterion, the resonance of the transducer has to be precisely matched to $m f_{\mathrm{laser}}$, which is difficult to meet for the narrow-band response of a standard IDT without chirp. For the chirped design employed here, this shortcoming can be elegantly overcome taking advantage of the tailorable emission band. A schematic of our setup is presented in Fig. 5(a). The mode-locked laser used in our experiments provides the electrical signal shown in blue in the upper panel of Fig. 5(b). In the Fourier analysis of this signal depicted in the lower panel, we identify the repetition rate $f_{\mathrm{laser}} =$ 80 MHz of the laser pulses. Moreover, 11 higher Fourier components are detected with comparable amplitude. For stroboscopic spectroscopy, we use a frequency band filter to isolate the third overtone at $4f_{\mathrm{laser}} = 320$ MHz, matching the $f_{\mathrm{SAW},2}$ frequency band of IDT2. The filtered signal and its Fourier transform are plotted in red in Fig. 5(b). We adjust the power level of the frequency filter signal using a variable attenuator. This signal is amplified to a constant power level of $P_{\mathrm{rf}} = +24$ dBm, directly applied to IDT2 to excite a SAW. Thus, the relative phase (i.e., temporal delay) between the SAW and the train of laser pulses is stably locked. Next, we demonstrate tuning of this relative phase by either introducing a temporal delay in the electrical $\Delta t_{\mathrm{electrical}}$ or optical branch $\Delta t_{\mathrm{optical}}$ of the setup. As shown

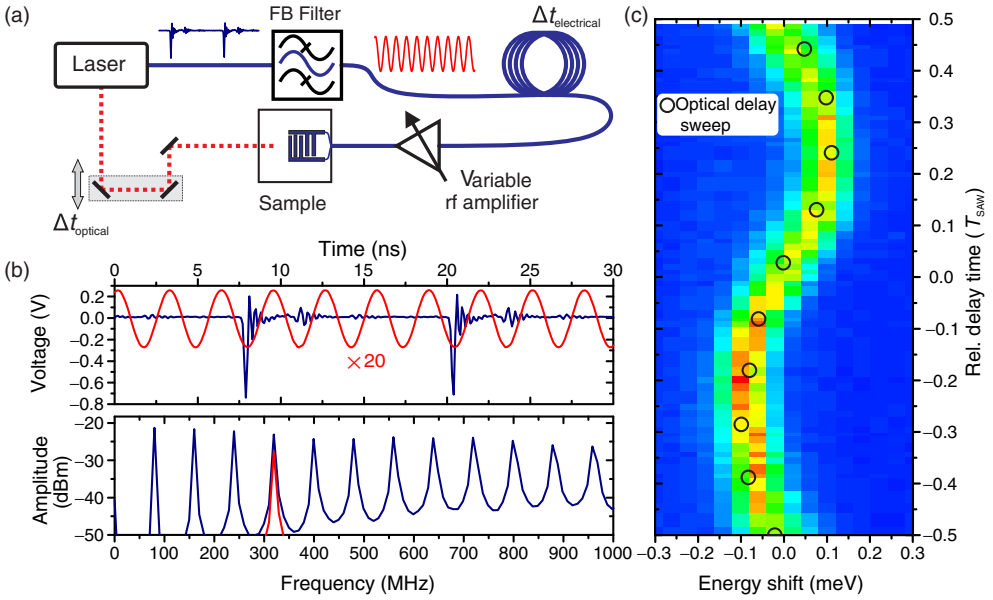

FIG. 5 Stroboscopic spectroscopy. (a) Implementation: The monitor output of a mode-locked fibre laser is passed through a frequency-band filter (FB filter) to isolate $f_{\mathrm{rf}} = 4f_{\mathrm{laser}} = 320$ MHz. The electrical signal is attenuated to a constant power level amplified to $P_{\mathrm{rf}} = +24$ dBm and finally applied to IDT2. The temporal delay between the excited SAW and the train of laser pulses is tuned either electrically by a cable-based delay ($\Delta t_{\mathrm{electrical}}$) or optically by variation of the propagation length of the laser beam ($\Delta t_{\mathrm{optical}}$). (b) Upper panel: Electrical signal directly from of the laser monitor output (blue) and frequency filtered (red) after passing through the FB filter. Lower panel: FFT amplitude of the monitor signal (blue) consisting of f_{laser} and 11 overtones and the filtered signal (red) containing only a single component $4f_{\mathrm{laser}}$. (c) Time-integrated emission spectra recorded from a single sensor QD as a function of $\Delta t_{\mathrm{electrical}}$ (at fixed $\Delta t_{\mathrm{optical}}$) plotted in false-color representation. The independently measured $\Delta E(\Delta t_{\mathrm{optical}})$ for fixed $\Delta t_{\mathrm{electrical}}$ is overlaid as open symbols. The characteristic sinusoidal modulation induced by the dynamic acoustic field of the SAW is faithfully reproduced in both independent and complementary experiments.

in Fig. 5(a), $\Delta t_{\text{electrical}}$ is controlled by introducing cable-based electrical delays. The cable-length-dependent losses in this scheme require the two-stage power-level control using a variable attenuator and a constant gain amplifier. Two typical stroboscopic scans recorded from a single sensor QD are presented in Fig. 5(c). For the $\Delta t_{\text{electrical}}$ scan, the emission intensity is color coded and plotted as a function of spectral shift relative to the unperturbed energy of the emitted photon and the programmed temporal delay over a full acoustic cycle. In these data, we resolve clearly the expected dynamic modulation of the QD emission energy by the oscillating acoustic field of the SAW [9,45]. As mentioned before, no signatures of dynamic charge-state programming are resolved in the data. Furthermore, we independently confirm a tunable temporal delay in the optical branch $\Delta t_{\text{optical}}$ by varying the optical propagation length of the laser pulses while keeping $\Delta t_{\text{electrical}}$ constant [61]. From the obtained data, we extract the QD emission energies as a function of $\Delta t_{\text{optical}}$. Such measured QD emission energies for ten values of $\Delta t_{\text{optical}}$ equally distributed over one acoustic cycle are plotted as symbols in Fig. 5(c). These independently measured QD emission energies programmed by tuning $\Delta t_{\text{optical}}$ faithfully follow the oscillation measured by variation of $\Delta t_{\text{electrical}}$. These combined experiments nicely confirm the reciprocity of our two independent approaches to tune the relative phase between the SAW and the laser pulses.

IV. PHASE-LOCKED EXCITATION AND TIME-RESOLVED DETECTION

Finally, we demonstrate full time-domain spectroscopy by combining phase-locked optical excitation and time-resolved detection of the QD emission in the same experiment. The implemented experimental scheme is shown schematically in Fig. 6(a). The laser reference signal is sent to a −3-dB (50:50) rf beam splitter. One port of this beam splitter is connected to IDT2 to generate a SAW at $4f_{\text{laser}} = 320$ MHz. Again, the temporal delay between the SAW and the laser pulses exciting the QD (red dashed line) is tuned electrically. The emission of the QD (green dashed line) is spectrally filtered by a monochromator and detected by a single-photon avalanche detector (SPAD) [42]. The second port of the rf beam splitter and the electrical output of the SPAD are directly connected to the inputs of a time-correlated single-photon-counting (TCSPC) module. The expected temporal evolution is shown schematically on the right of Fig. 6(a). Here, we assume a sinusoidally modulated emission line. The system is optically excited at approximately $0.4T_{\text{SAW}}$ and decays exponentially with a time constant of $\tau \approx 0.5T_{\text{SAW}}$. The

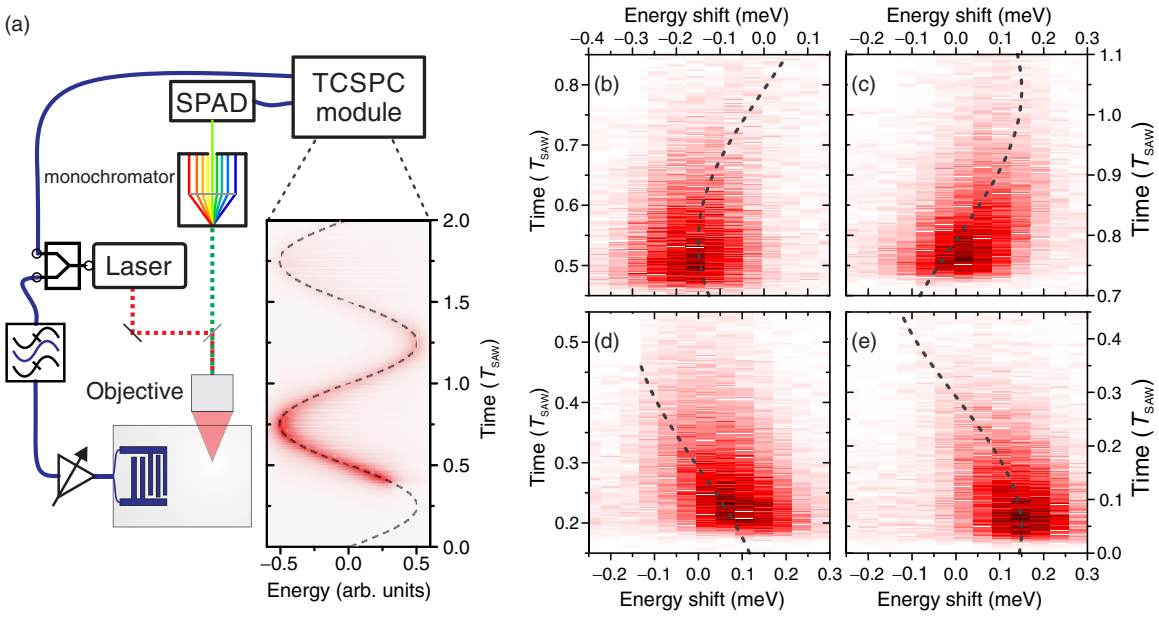

FIG. 6 Phase-locked excitation and time-resolved detection. (a) Implementation: The monitor output of a mode-locked fiber laser is split by a −3-dB rf beam splitter. One output is passed through a frequency-band filter (FB filter) to isolate $f_{\text{rf}} = 4f_{\text{laser}} = 320$ MHz, attenuated, amplified, and connected to IDT2. The emission of a sensor QD is detected by a SPAD. The detector signal is time correlated with the laser monitor signal from the second output of the rf beam splitter using a TCSPC module. The predicted time- and spectrally resolved emission spectra of a QD is shown in false-color representation on the right. (b)–(e) Time-resolved emission spectra of a single sensor QD recorded for four independently set values of $\Delta t_{\text{electrical}}$. The SPAD counts are color coded and plotted as a function of ΔE and time t during the acoustic cycle. The detected spectral evolution faithfully follows the dynamic modulation by the SAW and the modulation observed by time-integrated stroboscopy (dotted line) shown in Fig. 5.

signal intensity is color coded and plotted as a function of time (vertical axis) and photon energy (horizontal axis). This model predicts that in such an experiment, the time evolution of the QD emission is directly resolvable. Figures 6(b)–6(e) demonstrates phase-locked excitation and time- and spectrally resolved detection for four different times of photoexcitation $\Delta t_{\mathrm{electrical}}$ distributed over one acoustic cycle (3.125 ns). The TCSPC counts are normalized for each $\Delta t_{\mathrm{electrical}}$ and plotted color coded as a function of energy shift and absolute time during the acoustic cycle. In contrast to the modeled emission behavior shown in Fig. 6(a), here the PL decay time of the QD $\tau_{\mathrm{PL}} \approx 0.32$ ns $\approx 0.1 T_{\mathrm{SAW}}$. Thus, the expected temporal modulation is resolved only in a relatively short time interval after photoexcitation. The temporal modulation of the QD emission line derived from our stroboscopy data is plotted as a solid dashed line. Clearly, all four spectral and temporal evolutions of the emission signal precisely follow the stroboscopy data (dashed line): in Fig. 6(b), photoexcitation occurs at $\Delta t_{\mathrm{electrical}} \approx 0.4 T_{\mathrm{SAW}}$, slightly before the maximum of the spectral modulation. Under this excitation condition, no pronounced spectral shift of the emission is observed because the emission line remains approximately fixed in the spectral domain within the decay time of the QD. This time evolution changes dramatically as $\Delta t_{\mathrm{electrical}}$ increases by approximately $0.25 T_{\mathrm{SAW}}$ in Fig. 6(c). Under these excitation conditions, the emission line shifts rapidly towards higher photon energies. The shift rate is sufficiently large and leads to the pronounced spectral shift within τ_{PL} as observed in our data. The direction of this shift changes in Fig. 6(d). Here, the QD is excited on the falling slope of the modulation, again in excellent agreement with the experimental observation. Finally, Fig. 6(e) presents data for $\Delta t_{\mathrm{electrical}} \approx 0.05 T_{\mathrm{SAW}}$ set almost exactly to the maximum of the spectral modulation. Here, the emission line initially remains constant and starts to shift to lower photon energy as the shift rate starts to increase. These observations prove that the emission energy is shifted on time scales shorter than the lifetime of the probed emitters. We note that for $\tau_{\mathrm{PL}} \geq 0.5 T_{\mathrm{SAW}}$, time-resolved detection is imperative: in a simple stroboscopic experiment, the observed time-integrated emission converges to that of the phase-averaged case demonstrated in Fig. 2.

V. CONCLUSIONS AND PERSPECTIVES

In conclusion, we demonstrate a versatile scheme to realize stable phase locking between the train of optical pulses emitted by a mode-locked laser and a radio-frequency SAW. Our scheme relies on properly designed transducers, which combine a multiharmonic architecture with a frequency chirp. This combination enables the excitation of SAWs over wide frequency bands for the fundamental SAW and its higher harmonics. Our demonstrated scheme will be the foundation for advanced SAW-based spectroscopy techniques, nanomechanical manipulation, and ultimately in acoustic quantum technologies. The frequency chirp is particularly powerful. Its wide passband enables a stable phase lock between the acoustic signal and the coherent optical pulses emitted with a fixed repetition rate by a mode-locked laser. For conventional, narrow-band IDTs, even small deviations in the transducer fabrication detune $f_{\mathrm{SAW}} \neq m f_{\mathrm{laser}}$, such that no stable phase can be established. Apart from the QDs employed here and other types of quantum emitters [62], the demonstrated method is directly applicable both for acousto-optoelectronic spectroscopy to probe charge-carrier dynamics and mobilities [63–65], or phase-locked SAW-photoconductance spectroscopy and tomography [20,66–68]. It will prove particularly useful for any system relying on coherent and resonant optical excitation and probing its acoustically imprinted dynamics on ultrafast time scales, including SAW-driven Landau-Zener gates [49] or exciton-photon-polariton condensates in microcavities [69,70]. Moreover, in fused $LiNbO_3$-photodiode hybrids [71], our concept will allow unified electrical and acoustic control ultimately on subnanosecond time scales [72–74]. In the emerging field of optomechanics, the recently demonstrated mutually coherent control of optomechanical resonators [34] by coherent SAWs and optical fields can be extended to pulsed optical excitation schemes. Moreover, our chirp design overcomes a native limitation of nonchirped multiharmonic transducers: the mass loading by the metal electrodes of the transducer leads to a frequency-dependent shift of SAW phase velocity underneath the transducer and, thus, to a change of the resonance frequency. So, for higher harmonics, the relation $f_{\mathrm{SAW},n} = n f_{\mathrm{SAW},1}$ is no longer valid, rendering multicomponent spanning additive Fourier synthesis [9] extremely challenging. This shortcoming is no longer present for the IDT design presented here, paving the way to arbitrary waveform synthesis over the entire hypersonic frequency domain. Such tailored phonon fields enable coherent control schemes in SAW-resonator-based quantum acoustics [48] or theoretically conceived SAW-driven quantum gates [49].

ACKNOWLEDGMENTS

This work is supported by the Deutsche Forschungsgemeinschaft (DFG) via the Emmy Noether Program (KR3790/2-1) and the Cluster of Excellence "Nanosystems Initiative Munich." A. R. acknowledges support from the Linz Institute of Technology and the Austrian Science Fund (FWF): P29603.

APPENDIX A: SAMPLE DESIGN

The (Al,Ga)As heterostructure used in our experiment contains a single layer of strain-free GaAs QDs embedded in (Al,Ga)As barriers fabricated by a Ga-droplet etching technique [52]. The full details on the heterostructure can

be found in Ref. [9]. IDTs (Ti 5 nm/Al 50 nm) are monolithically fabricated directly on the GaAs-based heterostructure in a lift-off process using a resist mask patterned by electron-beam lithography.

APPENDIX B: IDT DESIGN

The IDT design is derived from an impulse model [59,60]. Here, every finger n of the IDT is considered as the source of a plane wave $A_n \exp[i2\pi f(x_n/c_{\mathrm{SAW}})]$. In this expression, x_n is the position of the nth finger. A_n is the amplitude of the wave and reflects the polarity of the different fingers of the IDT. The frequency response is then obtained by summation over all fingers n of the IDT $\sum_n A_n \exp[i2\pi f(x_n/c_{\mathrm{SAW}})]$. We employ the same model to derive the chirp-free multiharmonic design in Ref. [9].

APPENDIX C: EXPERIMENTAL DETAILS

All experiments are performed at $T = 4$ K in a closed-cycle helium cryostat equipped with a low-temperature photonic probe station (attocube, Munich, Germany). Charge carriers are photogenerated by pulsed-laser sources focused to a diffraction-limited spot by a NA = 0.81 low-temperature microscope objective (LT-APO/NIR/0.81, attocube, Munich, Germany). Emission from single QDs is collected by the same objective and dispersed in a 0.75-m grating monochromator and detected either by a liquid-nitrogen-cooled charge-coupled device for multichannel time-integrated spectrum acquisition or a SPAD for single-channel, time-resolved detection.

1. Radio-frequency scans

For experiments in which f_{rf} is tuned (Figs. 3 and 4), a diode laser emitting approximately 90-ps-long pulses with a wavelength of 660 nm is triggered with a repetition rate $f_{\mathrm{laser}} = 80$ MHz. The rf voltage output of a signal generator is amplified to a constant power level of $P_{\mathrm{rf}} = +24$ dBm and connected to the IDT. The driving signal is applied as $\Delta t = 2000$ ns long pulses to reduce heating of the sample [41]. The electrical pulses triggering the pulsed laser are active only during the time the SAW propagates across the position of the QD [40]. f_{laser} and rate f_{rf} are incommensurate ($f_{\mathrm{rf}} \neq m f_{\mathrm{laser}}$, m being an integer) to average the dynamic modulation of the QD over a full rf cycle in a single time-integrated spectrum [71].

2. Phase-locked excitation with tunable laser of fixed repetition rate

Figure 7 shows the full setup for stroboscopy using a mode-locked laser (cf. Fig. 5). A mode-locked tunable fiber laser (TOPTICA Photonics AG, Gräfelfing, Germany) emitting <1-ps pulses with a fixed repetition rate $f_{\mathrm{laser}} = 80$ MHz of wavelength 640 nm is used for optical excitation. SAW generation is realized as described in the main text. In essence, a frequency bandpass filter (Mini-Circuits SXBP-310+) isolates the $4f_{\mathrm{laser}} = 320$ MHz component of the Nuclear Instrumentation Module (NIM) pulse electrical monitor output of the laser. Tuning of $\Delta t_{\mathrm{electrical}}$ is set by a cascade of two cable-based electrical delay systems (Ortec, Modell 425). For each set $\Delta t_{\mathrm{electrical}}$, the electrical power is adjusted to $P_{\mathrm{rf}} = -10$ dBm by using a constant gain amplifier (Mini-Circuits, ZFSC-2-372-S+) and two digital step attenuators (Mini-Circuits, ZFAT-R512 and ZFAT-124) to compensate for the inevitable cable-length-dependent losses and to ensure SAW generation with $P_{\mathrm{rf}} = +24$ dBm after amplification by +34 dB using a second constant gain amplifier (Mini-Circuits, ZFSC-2-372-S+). In order to monitor the electrical power, the signal is split by a −3-dB rf beam splitter (Mini-Circuits, ZFSC-2-372-S+) before final amplification and analyzed by a 2-GHz-bandwidth digital-storage oscilloscope (Teledyne LeCroy, Waverunner 620Zi). Furthermore, the oscilloscope is used to determine the exact relative phase between the electrically excited SAW and the optical excitation using a high-speed photodetector (Newport, 818-BB-21) to monitor the optical output of the laser. Tuning of $\Delta t_{\mathrm{optical}}$ is realized manually by variation of the length of the optical excitation path. For all stroboscopic

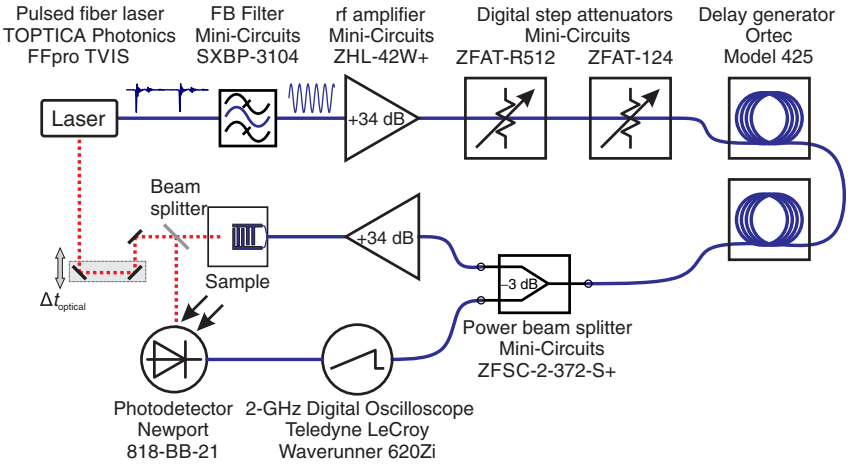

FIG. 7 Detailed schematic of the setup used for the full phase-locked excitation and time-integrated detection [data shown in Fig. 5(c)]. The electrical signal is depicted by the blue connections and the optical by the red ones.

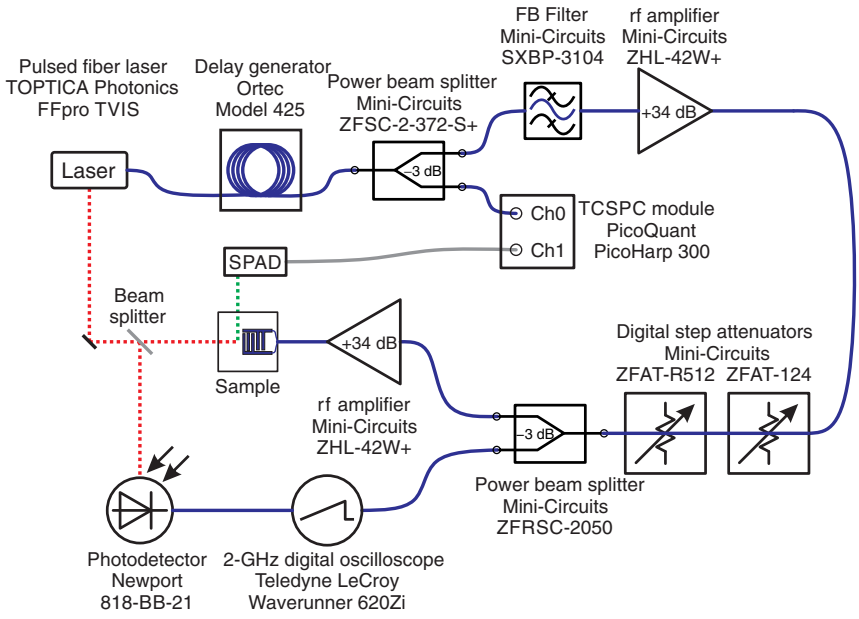

FIG. 8 Detailed schematic of the setup used for the full phase-locked excitation and time-resolved detection [data shown in Figs. 6(b)–6(e)]. The electrical signal is depicted by the blue connections and the optical by the red ones.

data shown in Fig. 5(c), time-integrated multichannel detection is used.

Figure 8 shows a schematic of the full setup for the full phase-locked excitation and time-resolved detection scheme (cf. Fig. 6). We scan the detection wavelength of the monochromator and record individual PL time transients using a Si single-photon-counting module connected to a two-channel TCSPC module (PicoQuant, PicoHarp 300) [32]. In addition, the electrical setup is slightly changed to meet the new requirements. Essentially, one additional −3-dB rf beam splitter (Mini-Circuits, ZFSC-2-372-S+) is used to obtain the reference signal for the TCSPC module. This is done before amplification and attenuation and after setting the electrical delay $\Delta t_{\text{electrical}}$ in order to match the input specifications of the TCSPC module and, at the same time, to resolve the set time delay in the time-resolved measurements.

[1] G. Kurizki, P. Bertet, Y. Kubo, K. Mølmer, D. Petrosyan, P. Rabl, and J. Schmiedmayer, Quantum technologies with hybrid systems, Proc. Natl. Acad. Sci. U.S.A. **112**, 3866 (2015).

[2] M. Schleier-Smith, Hybridizing Quantum Physics and Engineering, Phys. Rev. Lett. **117**, 100001 (2016).

[3] S. Kolkowitz, A. C. Bleszynski Jayich, Q. P. Unterreithmeier, S. D. Bennett, P. Rabl, J. G. E. Harris, and M. D. Lukin, Coherent sensing of a mechanical resonator with a single-spin qubit, Science **335**, 1603 (2012).

[4] A. Barfuss, J. Teissier, E. Neu, A. Nunnenkamp, and P. Maletinsky, Strong mechanical driving of a single electron spin, Nat. Phys. **11**, 820 (2015).

[5] I. Yeo, P.-L. de Assis, A. Gloppe, E. Dupont-Ferrier, P. Verlot, N. S. Malik, E. Dupuy, J. Claudon, J.-M. Gérard, A. Auffèves, G. Nogues, S. Seidelin, J.-P. Poizat, O. Arcizet, and M. Richard, Strain-mediated coupling in a quantum dot–mechanical oscillator hybrid system, Nat. Nanotechnol. **9**, 106 (2013).

[6] M. Montinaro, G. Wüst, M. Munsch, Y. Fontana, E. Russo-Averchi, M. Heiss, A. Fontcuberta i Morral, R. J. Warburton, and M. Poggio, Quantum dot opto-mechanics in a fully self-assembled nanowire, Nano Lett. **14**, 4454 (2014).

[7] J. D. Teufel, T. Donner, D. Li, J. W. Harlow, M. S. Allman, K. Cicak, A. J. Sirois, J. D. Whittaker, K. W. Lehnert, and R. W. Simmonds, Sideband cooling of micromechanical motion to the quantum ground state, Nature (London) **475**, 359 (2011).

[8] R. M. White and F. W. Voltmer, Direct piezoelectric coupling to surface elastic waves, Appl. Phys. Lett. **7**, 314 (1965).

[9] F. J. R. Schülein, E. Zallo, P. Atkinson, O. G. Schmidt, R. Trotta, A. Rastelli, A. Wixforth, and H. J. Krenner, Fourier synthesis of radiofrequency nanomechanical pulses with different shapes, Nat. Nanotechnol. **10**, 512 (2015).

[10] C. K. Campbell, *Surface Acoustic Wave Devices for Mobile and Wireless Communications* (Academic Press, San Diego, CA, 1998).

[11] D. P. Morgan, *Surface Acoustic Wave Filters: With Applications to Electronic Communications and Signal Processing*, 2nd ed. (Academic Press, Amsterdam, 2007).

[12] A. Wixforth, J. P. Kotthaus, and G. Weimann, Quantum Oscillations in the Surface-Acoustic-Wave Attenuation Caused by a Two-Dimensional Electron System, Phys. Rev. Lett. **56**, 2104 (1986).

[13] R. Willett, M. Paalanen, R. Ruel, K. West, L. Pfeiffer, and D. Bishop, Anomalous Sound Propagation at $\nu = 1/2$ in a 2D Electron Gas: Observation of a Spontaneously Broken Translational Symmetry?, Phys. Rev. Lett. **65**, 112 (1990).

[14] I. V. Kukushkin, J. H. Smet, V. W. Scarola, V. Umansky, and K. von Klitzing, Dispersion of the excitations of fractional quantum Hall states, Science **324**, 1044 (2009).

[15] C. Rocke, S. Zimmermann, A. Wixforth, J. P. Kotthaus, G. Böhm, and G. Weimann, Acoustically Driven Storage of Light in a Quantum Well, Phys. Rev. Lett. **78**, 4099 (1997).

[16] F. Alsina, P. V. Santos, R. Hey, A. García-Cristóbal, and A. Cantarero, Dynamic carrier distribution in quantum wells modulated by surface acoustic waves, Phys. Rev. B **64**, 041304(R) (2001).

[17] V. Talyanskii, J. Shilton, M. Pepper, C. Smith, C. Ford, E. Linfield, D. Ritchie, and G. Jones, Single-electron transport in a one-dimensional channel by high-frequency surface acoustic waves, Phys. Rev. B **56**, 15180 (1997).

[18] J. Ebbecke, C. J. Strobl, and A. Wixforth, Acoustoelectric current transport through single-walled carbon nanotubes, Phys. Rev. B **70**, 233401 (2004).

[19] L. Bandhu, L. M. Lawton, and G. R. Nash, Macroscopic acoustoelectric Charge transport in graphene, Appl. Phys. Lett. **103**, 133101 (2013).

[20] E. Preciado, F. J. R. Schülein, A. E. Nguyen, D. Barroso, M. Isarraraz, G. von Son, I.-H. Lu, W. Michailow, B. Möller, V. Klee, J. Mann, A. Wixforth, L. Bartels, and H. J. Krenner, Scalable fabrication of a hybrid field-effect and acousto-electric device by direct growth of monolayer $MoS_2/LiNbO_3$, Nat. Commun. **6**, 8593 (2015).

[21] T. Sogawa, P. V. Santos, S. K. Zhang, S. Eshlaghi, A. D. Wieck, and K. H. Ploog, Transport and Lifetime Enhancement of Photoexcited Spins in GaAs by Surface Acoustic Waves, Phys. Rev. Lett. **87**, 276601 (2001).

[22] J. A. H. Stotz, R. Hey, P. V. Santos, and K. H. Ploog, Coherent spin transport through dynamic quantum dots, Nat. Mater. **4**, 585 (2005).

[23] S. Hermelin, S. Takada, M. Yamamoto, S. Tarucha, A. D. Wieck, L. Saminadayar, C. Bäuerle, and T. Meunier, Electrons surfing on a sound wave as a platform for quantum optics with flying electrons, Nature (London) **477**, 435 (2011).

[24] R. P. G. McNeil, M. Kataoka, C. J. B. Ford, C. H. W. Barnes, D. Anderson, G. A. C. Jones, I. Farrer, and D. A. Ritchie, On-demand single-electron transfer between distant quantum dots, Nature (London) **477**, 439 (2011).

[25] M. V. Gustafsson, P. V. Santos, G. Johansson, and P. Delsing, Local probing of propagating acoustic waves in a gigahertz echo chamber, Nat. Phys. **8**, 338 (2012).

[26] B. Bertrand, S. Hermelin, S. Takada, M. Yamamoto, S. Tarucha, A. Ludwig, A. D. Wieck, C. Bäuerle, and T. Meunier, Fast spin information transfer between distant quantum dots using individual electrons, Nat. Nanotechnol. **11**, 672 (2016).

[27] M. V. Gustafsson, T. Aref, A. F. Kockum, M. K. Ekstrom, G. Johansson, and P. Delsing, Propagating phonons coupled to an artificial atom, Science **346**, 207 (2014).

[28] D. A. Golter, T. Oo, M. Amezcua, K. A. Stewart, and H. Wang, Optomechanical Quantum Control of a Nitrogen-Vacancy Center in Diamond, Phys. Rev. Lett. **116**, 143602 (2016).

[29] M. M. de Lima, Jr. and P. V. Santos, Modulation of photonic structures by surface acoustic waves, Rep. Prog. Phys. **68**, 1639 (2005).

[30] D. A. Fuhrmann, S. M. Thon, H. Kim, D. Bouwmeester, P. M. Petroff, A. Wixforth, and H. J. Krenner, Dynamic modulation of photonic crystal nanocavities using gigahertz acoustic phonons, Nat. Photonics **5**, 605 (2011).

[31] S. A. Tadesse, H. Li, Q. Liu, and M. Li, Acousto-optic modulation of a photonic crystal nanocavity with lamb waves in microwave *K* band, Appl. Phys. Lett. **107**, 201113 (2015).

[32] S. Kapfinger, T. Reichert, S. Lichtmannecker, K. Müller, J. J. Finley, A. Wixforth, M. Kaniber, and H. J. Krenner, Dynamic acousto-optic control of a strongly coupled photonic molecule, Nat. Commun. **6**, 8540 (2015).

[33] J. Bochmann, A. Vainsencher, D. D. Awschalom, and A. N. Cleland, Nanomechanical coupling between microwave and optical photons, Nat. Phys. **9**, 712 (2013).

[34] K. C. Balram, M. I. Davanço, J. D. Song, and K. Srinivasan, Coherent coupling between radiofrequency, optical and acoustic waves in piezo-optomechanical circuits, Nat. Photonics **10**, 346 (2016).

[35] A. Vainsencher, K. J. Satzinger, G. A. Peairs, and A. N. Cleland, Bi-directional conversion between microwave and optical frequencies in a piezoelectric optomechanical device, Appl. Phys. Lett. **109**, 033107 (2016).

[36] K. C. Balram, M. I. Davanço, B. R. Ilic, J.-H. Kyhm, J. D. Song, and K. Srinivasan, Acousto-Optic Modulation and Optoacoustic Gating in Piezo-Optomechanical Circuits, Phys. Rev. Applied **7**, 024008 (2017).

[37] C. Wiele, F. Haake, C. Rocke, and A. Wixforth, Photon trains and lasing: The periodically pumped quantum dot, Phys. Rev. A **58**, R2680 (1998).

[38] O. D. D. Couto, S. Lazić, F. Iikawa, J. A. H. Stotz, U. Jahn, R. Hey, and P. V. Santos, Photon anti-bunching in acoustically pumped quantum dots, Nat. Photonics **3**, 645 (2009).

[39] S. Lazić, R. Hey, and P. V. Santos, Mechanism of non-classical light emission from acoustically populated (311)A GaAs quantum wires, New J. Phys. **14**, 013005 (2012).

[40] S. Völk, F. J. R. Schülein, F. Knall, D. Reuter, A. D. Wieck, T. A. Truong, H. Kim, P. M. Petroff, A. Wixforth, and H. J. Krenner, Enhanced sequential carrier capture into individual quantum dots and quantum posts controlled by surface acoustic waves, Nano Lett. **10**, 3399 (2010).

[41] S. Völk, F. Knall, F. J. R. Schülein, T. A. Truong, H. Kim, P. M. Petroff, A. Wixforth, and H. J. Krenner, Direct observation of dynamic surface acoustic wave controlled carrier injection into single quantum posts using phase-resolved optical spectroscopy, Appl. Phys. Lett. **98**, 023109 (2011).

[42] F. J. R. Schülein, K. Müller, M. Bichler, G. Koblmüller, J. J. Finley, A. Wixforth, and H. J. Krenner, Acoustically regulated carrier injection into a single optically active quantum dot, Phys. Rev. B **88**, 085307 (2013).

[43] M. Weiß, J. B. Kinzel, F. J. R. Schülein, M. Heigl, D. Rudolph, S. Morkötter, M. Döblinger, M. Bichler, G. Abstreiter, J. J. Finley, G. Koblmüller, A. Wixforth, and H. J. Krenner, Dynamic acoustic control of individual optically active quantum dot-like emission centers in heterostructure nanowires, Nano Lett. **14**, 2256 (2014).

[44] M. Weiß, F. J. R. Schülein, J. B. Kinzel, M. Heigl, D. Rudolph, M. Bichler, G. Abstreiter, J. J. Finley, A. Wixforth, G. Koblmüller, and H. J. Krenner, Radio frequency occupancy state control of a single nanowire quantum dot, J. Phys. D. **47**, 394011 (2014).

[45] J. R. Gell, M. B. Ward, R. J. Young, R. M. Stevenson, P. Atkinson, D. Anderson, G. A. C. Jones, D. A. Ritchie, and A. J. Shields, Modulation of single quantum dot energy levels by a surface-acoustic-wave, Appl. Phys. Lett. **93**, 081115 (2008).

[46] M. Metcalfe, S. M. Carr, A. Muller, G. S. Solomon, and J. Lawall, Resolved Sideband Emission of InAs/GaAs Quantum Dots Strained by Surface Acoustic Waves, Phys. Rev. Lett. **105**, 0037401 (2010).

[47] B. Villa, A. J. Bennett, D. J. P. Ellis, J. P. Lee, J. Skiba-Szymanska, T. A. Mitchell, J. P. Griffiths, I. Farrer, D. A. Ritchie, C. J. B. Ford, and A. J. Shields, Surface acoustic wave modulation of a coherently driven quantum dot in a pillar microcavity, Appl. Phys. Lett. **111**, 011103 (2017).

[48] M. J. A. Schuetz, E. M. Kessler, G. Giedke, L. M. K. Vandersypen, M. D. Lukin, and J. I. Cirac, Universal Quantum Transducers Based on Surface Acoustic Waves, Phys. Rev. X **5**, 0031031 (2015).

[49] R. Blattmann, H. J. Krenner, S. Kohler, and P. Hänggi, Entanglement creation in a quantum-dot–nanocavity system by Fourier-synthesized acoustic pulses, Phys. Rev. A **89**, 0012327 (2014).

[50] M. Weiß, S. Kapfinger, T. Reichert, J. J. Finley, A. Wixforth, M. Kaniber, and H. J. Krenner, Surface acoustic wave regulated single photon emission from a coupled quantum dot–nanocavity system, Appl. Phys. Lett. **109**, 033105 (2016).

[51] R. H. Tancrell, M. B. Schulz, H. H. Barrett, L. Davis, and M. G. Holland, Dispersive delay lines using ultrasonic surface waves, Proc. IEEE **57**, 1211 (1969).

[52] P. Atkinson, E. Zallo, and O. G. Schmidt, Independent wavelength and density control of uniform GaAs/AlGaAs quantum dots grown by infilling self-assembled nanoholes, J. Appl. Phys. **112**, 054303 (2012).

[53] W. R. Smith, H. M. Gerard, and W. R. Jones, Analysis and design of dispersive interdigital surface-wave transducers, IEEE Trans. Microwave Theory Tech. **20**, 458 (1972).

[54] F. J. R. Schülein, J. Pustiowski, K. Müller, M. Bichler, G. Koblmüller, J. J. Finley, A. Wixforth, and H. J. Krenner, Surface acoustic wave controlled charge dynamics in a thin InGaAs quantum well, JETP Lett. **95**, 575 (2012).

[55] R. Heitz, M. Veit, N. Ledentsov, A. Hoffmann, D. Bimberg, V. Ustinov, P. Kop'ev, and Z. Alferov, Energy relaxation by multiphonon processes in InAs/GaAs quantum dots, Phys. Rev. B **56**, 10435 (1997).

[56] S. Trumm, M. Wesseli, H. J. Krenner, D. Schuh, M. Bichler, J. J. Finley, and M. Betz, Spin-preserving ultrafast carrier capture and relaxation in InGaAs quantum dots, Appl. Phys. Lett. **87**, 153113 (2005).

[57] A. Violante, K. Cohen, S. Lazić, R. Hey, R. Rapaport, and P. V. Santos, Dynamics of indirect exciton transport by moving acoustic fields, New J. Phys. **16**, 033035 (2014).

[58] E. D. S. Nysten, Y. H. Huo, H. Yu, G. F. Song, A. Rastelli, and H. J. Krenner, Multi-harmonic quantum dot optomechanics in fused $LiNbO_3-(Al)GaAs$ hybrids, J. Phys. D **50**, 43LT01 (2017).

[59] R. H. Tancrell and M. G. Holland, Acoustic surface wave filters, Proc. IEEE **59**, 393 (1971).

[60] H. Matthews, *Surface Wave Filters* (Wiley, New York, 1977).

[61] C. Ruppert, F. Förster, A. Zrenner, J. B. Kinzel, A. Wixforth, H. J. Krenner, and M. Betz, Radio frequency electromechanical control over a surface plasmon polariton coupler, ACS Photonics **1**, 91 (2014).

[62] D. A. Golter, T. Oo, M. Amezcua, I. Lekavicius, K. A. Stewart, and H. Wang, Coupling a Surface Acoustic Wave to an Electron Spin in Diamond via a Dark State, Phys. Rev. X **6**, 041060 (2016).

[63] J. B. Kinzel, F. J. R. Schülein, M. Weiß, L. Janker, D. D. Bühler, M. Heigl, D. Rudolph, S. Morkötter, M. Döblinger, M. Bichler, G. Abstreiter, J. J. Finley, A. Wixforth, G. Koblmüller, and H. J. Krenner, The native material limit of electron and hole mobilities in semiconductor nanowires, ACS Nano **10**, 4942 (2016).

[64] A. García-Cristóbal, A. Cantarero, F. Alsina, and P. V. Santos, Spatiotemporal carrier dynamics in quantum wells under surface acoustic waves, Phys. Rev. B **69**, 205301 (2004).

[65] T. Sogawa, H. Sanada, H. Gotoh, H. Yamaguchi, S. Miyashita, and P. V. Santos, Photoluminescence dynamics of GaAs/AlAs quantum wells modulated by surface acoustic waves, Jpn. J. Appl. Phys. **46**, L758 (2007).

[66] D. A. Fuhrmann, H. J. Krenner, A. Wixforth, A. Curran, K. A. Prior, R. J. Warburton, and J. Ebbecke, Noninvasive probing of persistent conductivity in high quality ZnCdSe/ZnSe quantum wells using surface acoustic waves, J. Appl. Phys. **107**, 093717 (2010).

[67] T. Poole, L. Bandhu, and G. R. Nash, Acoustoelectric photoresponse in graphene, Appl. Phys. Lett. **106**, 133107 (2015).

[68] M. Streibl, A. Wixforth, J. P. Kotthaus, A. O. Govorov, C. Kadow, and A. C. Gossard, Imaging of acoustic charge transport in semiconductor heterostructures by surface acoustic waves, Appl. Phys. Lett. **75**, 4139 (1999).

[69] M. de Lima, M. van der Poel, P. Santos, and J. Hvam, Phonon-Induced Polariton Superlattices, Phys. Rev. Lett. **97**, 045501 (2006).

[70] E. A. Cerda-Méndez, D. N. Krizhanovskii, M. Wouters, R. Bradley, K. Biermann, K. Guda, R. Hey, P. V. Santos, D. Sarkar, and M. S. Skolnick, Polariton Condensation in Dynamic Acoustic Lattices, Phys. Rev. Lett. **105**, 116402 (2010).

[71] J. Pustiowski, K. Müller, M. Bichler, G. Koblmüller, J. J. Finley, A. Wixforth, and H. J. Krenner, Independent dynamic acousto-mechanical and electrostatic control of individual quantum dots in a $LiNbO_3$-GaAs hybrid, Appl. Phys. Lett. **106**, 013107 (2015).

[72] S. Michaelis de Vasconcellos, S. Gordon, M. Bichler, T. Meier, and A. Zrenner, Coherent control of a single exciton qubit by optoelectronic manipulation, Nat. Photonics **4**, 545 (2010).

[73] J. Zhang, F. Ding, E. Zallo, R. Trotta, B. Höfer, L. Han, S. Kumar, Y. Huo, A. Rastelli, and O. G. Schmidt, A nanomembrane-based wavelength-tunable high-speed single-photon-emitting diode, Nano Lett. **13**, 5808 (2013).

[74] F. Pagliano, Y. Cho, T. Xia, F. van Otten, R. Johne, and A. Fiore, Dynamically controlling the emission of single excitons in photonic crystal cavities, Nat. Commun. **5**, 5786 (2014).